

ORIGINAL ARTICLE

¹⁸F-FDG-PET/CT imaging in an IL-6- and MYC-driven mouse model of human multiple myeloma affords objective evaluation of plasma cell tumor progression and therapeutic response to the proteasome inhibitor ixazomib

K Duncan¹, TR Rosean^{1,2}, VS Tompkins¹, A Olivier¹, R Sompallae^{1,3}, F Zhan⁴, G Tricot⁴, MR Acevedo⁵, LLB Ponto⁵, SA Walsh⁵, LT Tygrett¹, AJ Berger⁶, T Waldschmidt¹, HC Morse III⁷, JJ Sunderland^{5,8} and S Janz^{1,8}

¹⁸F-fluorodeoxyglucose positron emission tomography (FDG-PET) and computed tomography (CT) are useful imaging modalities for evaluating tumor progression and treatment responses in genetically engineered mouse models of solid human cancers, but the potential of integrated FDG-PET/CT for assessing tumor development and new interventions in transgenic mouse models of human blood cancers such as multiple myeloma (MM) has not been demonstrated. Here we use BALB/c mice that contain the newly developed iMyc^{ΔE14} gene insertion and the widely expressed H2-L^d-IL6 transgene to demonstrate that FDG-PET/CT affords an excellent research tool for assessing interleukin-6- and MYC-driven plasma cell tumor (PCT) development in a serial, reproducible and stage- and lesion-specific manner. We also show that FDG-PET/CT permits determination of objective drug responses in PCT-bearing mice treated with the investigational proteasome inhibitor ixazomib (MLN2238), the biologically active form of ixazomib citrate (MLN9708), that is currently in phase 3 clinical trials in MM. Overall survival of 5 of 6 ixazomib-treated mice doubled compared with mice left untreated. One outlier mouse presented with primary refractory disease. Our findings demonstrate the utility of FDG-PET/CT for preclinical MM research and suggest that this method will play an important role in the design and testing of new approaches to treat myeloma.

Blood Cancer Journal (2013) 3, e165; doi:10.1038/bcj.2013.61; published online 29 November 2013

Keywords: GEMM (genetically engineered mouse model) of human cancer; preclinical cancer drug testing; plasma cell neoplasia

INTRODUCTION

The diagnosis, staging and therapeutic monitoring of multiple myeloma (MM), the second most common blood cancer in the United States, involves a variety of imaging methods that use either anatomy-based modalities (for example, conventional radiography including the whole-body radiographic series known as the metastatic bone survey¹ and computed tomography (CT)²), functional modalities (for example, positron emission tomography (PET)³, magnetic resonance imaging (MRI)⁴ and ^{99m}Tc-sestamibi⁵) or a combination of both modalities (for example, PET/CT).⁶ Integrated PET/CT, which is particularly useful for myeloma imaging,^{7,8} relies on positron-emitting radiopharmaceuticals, the most common of which is the glucose analog ¹⁸F-fluorodeoxyglucose (FDG).⁹ The utility of FDG is based on the Warburg effect, that is, the ability of MM and virtually all other cancer cells to undergo *aerobic* glycolysis that results in heightened glucose utilization and FDG uptake rates.¹⁰ FDG-PET/CT is a versatile imaging tool for MM because it assists diagnosis by virtue of identifying high tumor-yield biopsy sites;^{11,12} provides results superior to those of MBS for (1) staging

and restaging patients,¹³ (2) detecting extramedullary disease¹⁴ and (3) demonstrating treatment response;¹⁵ detects and localizes occult infection;¹⁶ and contributes to patient stratification, for example, by distinguishing patients with a complete imaging response before hematopoietic stem cell transplantation (superior survival) from patients with an incomplete response (inferior survival).¹⁷

In spite of these clinical benefits, FDG-PET/CT has not yet been embraced by the preclinical research community that employs mouse models of MM in which plasma cell tumors (PCTs) arise *de novo* in the presence of a normal immune system. These models include the archetypical, inflammation-induced peritoneal PCT in strain BALB/c mice;¹⁸ PCTs that arise in mice that carry either the Vκ*MYC,¹⁹ Eμ-Xbp1,²⁰ NPM-ALK,²¹ Eμ-Bcl2,²² H2-L^d-IL6,²³ Bcl-X_L^{24,25} or Sca1-MafB²⁶ transgenes; and anaplastic PCTs²⁷ that occur in Eμ-v-abl,²⁸ Myc (c-myc)^{29,30} and Eμ-Cnd1^{T286A} (see Gladden *et al.*³¹) transgenic (Tg) mice as well as in NSF.V⁺ congenics.³² To overcome certain limitations of these models, especially with regard to tumor onset (often too long) and genetic

¹Department of Pathology, University of Iowa Roy J and Lucille A Carver College of Medicine, Iowa City, IA, USA; ²The Interdisciplinary Immunology Graduate Program, University of Iowa Roy J and Lucille A Carver College of Medicine, Iowa City, IA, USA; ³The Bioinformatics Core Facility, University of Iowa Roy J and Lucille A Carver College of Medicine, Iowa City, IA, USA; ⁴Department of Internal Medicine, University of Iowa Roy J and Lucille A Carver College of Medicine, Iowa City, IA, USA; ⁵Department of Radiology, University of Iowa Roy J and Lucille A Carver College of Medicine, Iowa City, IA, USA; ⁶Takeda Pharmaceutica Company Ltd, Cambridge, MA, USA and ⁷Virology and Cellular Immunology Section, Laboratory of Immunogenetics, National Institutes of Allergy and Infectious Diseases, National Institutes of Health, Rockville, MD, USA. Correspondence: Professor JJ Sunderland, Department of Radiology, University of Iowa Roy J and Lucille A Carver College of Medicine, 3881 JPP, Iowa City, 52242 IA, USA or Professor S Janz, Department of Pathology, Carver College of Medicine, University of Iowa, 500 Newton Road, 1046C ML, Iowa City, 52242 IA, USA.

E-mail: john-sunderland@uiowa.edu or siegfried-janz@uiowa.edu

⁸These authors shared senior co-authorship.

Received 14 August 2013; revised 22 September 2013; accepted 2 October 2013

penetrance of the tumor phenotype (tumor incidence often too low), we and others have recently developed double-Tg strains, such as Bcl-X_LMyc³³ and IL6Myc,³⁴ in which tumor development is greatly accelerated (short onset) and fully penetrant (100% tumor incidence). However, the welcome feature of oncogene collaboration in these strains is accompanied by an unwelcome barrier to further improvement by crossing in one of the widely used Tg reporter genes of tumor development, for example, those encoding luciferase (enables *in vivo* bioluminescence imaging) or a fluorescent protein (enables *in vivo* fluorescence imaging). Breeding schemes to introduce a reporter gene onto a double-Tg background are laborious, time consuming and often prohibitively expensive.

In our current studies, we utilized an improved version of the IL6Myc model of human MM in which tumor progression is driven by a modified iMyc allele, designated iMyc^{ΔE_H},³⁵ but the same, widely expressed human interleukin-6 (IL-6) transgene³⁶ used in previous studies on IL6Myc-driven PCT.³⁴ Here we show that the reporter gene-independent imaging modality, FDG-PET/CT, is able to identify and quantitatively track the emergence and growth of myeloma-like tumors in these IL6Myc mice. In addition, FDG-PET was able to detect the response of the tumors during treatment with the proteasome inhibitor ixazomib that has previously demonstrated antitumor activity in preclinical models of plasma cell (PC) malignancy^{37,38} and in phase 1/2 trials of MM.³⁹ Our findings demonstrate the utility of FDG-PET/CT for preclinical MM research and suggest that this method will play an important role in testing new myeloma interventions.

MATERIALS AND METHODS

Mice

Double-transgenic (DTg) C.IL6Myc mice were selected from crosses of homozygous Tg C.iMyc^{ΔE_H} and heterozygous Tg C.H2-L^d-IL6 mice based on

genotyping of progeny. In accordance with a Mendelian trait, 50% of offspring exhibited the desired DTg genotype. Strain C.iMyc^{ΔE_H} is new; it was developed by gene targeting a his₆-tagged murine *Myc* cDNA 3' of the J_H region of the *Igh* locus, such that the intronic heavy-chain enhancer, E_H, was replaced by the inserted *Myc* gene, designated iMyc^{ΔE_H}.³⁵ The iMyc^{ΔE_H} transgene was backcrossed for more than 12 generations onto strain BALB/c (C) and then bred to homozygosity. The development and use of C.H2-L^d-IL6 congenic mice for research on the natural history of PCT has been described previously.²³ Tumor incidence in strain C.IL6Myc was determined as previously described.³⁴ All animal studies were approved under University of Iowa Institutional Animal Care and Use Committee Protocol 0701007.

Gene expression profiling, enzyme-linked immunosorbent assay, flow cytometry and serum protein electrophoresis

Global gene expression profiling relied on Illumina (San Diego, CA, USA) Mouse WG-6 v2.0 Bead Chips and data analytical approaches described elsewhere.⁴⁰ Serum immunoglobulin levels (enzyme-linked immunosorbent assay)⁴¹ and surface markers (flow cytometry)⁴² were analyzed as previously described. For serum protein electrophoresis, blood was collected either from live mice by submandibular vein puncture or at necropsy by heart puncture. Blood was transferred to EDTA-coated Microtainer tubes (Becton Dickinson, Franklin Lakes, NJ, USA) and spun for 5 min to obtain serum. Serum proteins were fractionated on Hydragel Protein(e) K20 gels using a Sebia (Norcross, GA, USA) electrophoresis chamber (90 V constant; 40 min migration time; 12 ± 3 mA). Densitometric analysis of electropherograms relied on ImageJ (NIH, Bethesda, MD, USA).

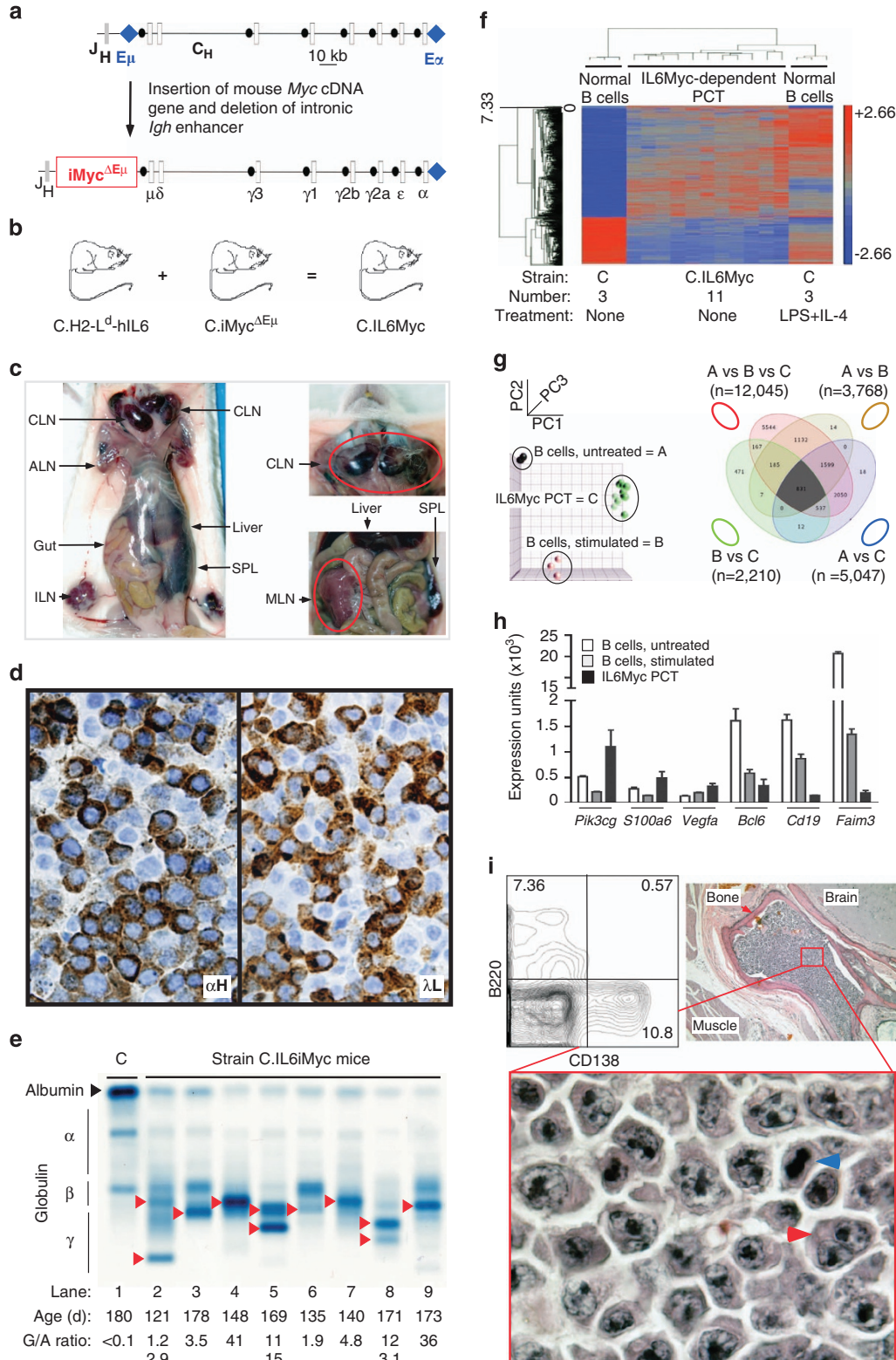
FDG-PET scanning

Mice in the tumor development study (nos. 1–15) were assigned to three different groups. Groups 1 and 2 contained age-matched DTg and normal C mice. Group 3 contained only DTg mice. Mice in the tumor treatment study (nos. 16–21) were included in one group. These mice received ixazomib (MLN2238) that was administered in the lateral tail vein at 7 mg/kg body weight. Ixazomib was dissolved in 5% hydroxypropyl-β-cyclodextrin. PET/CT scanning was performed after mice were fasted for

Figure 1. Features of PCTs arising in C.IL6/MYC mice. **(a)** Targeted Tg insertion of *Myc* in C.iMyc^{ΔE_H} mice. Shown are schemes of the normal mouse *Igh* locus (top) and the targeted *Igh* locus (bottom) harboring the inserted *Myc* gene (red box, not to scale) in the intervening genomic region between the Ig heavy-chain joining locus, J_H (gray rectangle), and the switch region (black dot) of the C_H locus (labeled open rectangle). The E_H and E_α enhancers are depicted by blue diamonds that are labeled. Note that E_H has been deleted during gene targeting so that only E_α is available to drive *Myc* expression in *cis*. The 'iMyc' transgene insertion site is also the preferred recombination site of chromosomal t(8;14)(q24;q32) *IGH-MYC* exchanges in human sporadic Burkitt lymphoma and chromosomal T(12;15) *Igh-Myc* exchanges in a subset of inflammation-dependent peritoneal plasmacytomas in strain C mice. **(b)** Generation of strain C.IL6Myc mice. The mice were selected from crosses of homozygous Tg (TG/TG) C.iMyc^{ΔE_H} mice and heterozygous Tg (TG/+) C.H2-L^d-IL6 mice. In accordance with a Mendelian trait, approximately half of offspring exhibited the desired doubly heterozygous Tg genotype. **(c)** Necropsy photographs of a PCT-bearing C.IL6Myc mouse before (left panel) and after (right panel) opening the abdominal wall. The mouse harbors enlarged, highly vascularized peripheral lymph nodes (LNs) in the CLN, ALN and ILN regions. The grossly enlarged MLN penetrating the gut loops and the moderately enlarged SPL become visible after removal of the abdominal wall. A mouse that developed hind leg paralysis is shown at bottom right. **(d)** Photomicrograph of a PCT found in an enlarged CLN of ~4-month-old C.IL6Myc mouse (hematoxylin and eosin (H&E); original magnification × 63). **(e)** Detection of paraproteins in sera of PCT-bearing C.IL6Myc mice (lanes 2–9). Lane 1 contains a sample from a normal control C mouse. Paraproteins (M-components, M-spikes) are indicated by red arrowheads pointing right, for example, IgG1/κ in lane 5 and IgA/κ in lane 7. Of 10 M-spikes isotyped by enzyme-linked immunosorbent assay (ELISA), 5 were found to be IgG1, 3 were IgG2b, 1 was IgG3 and 1 was IgA. The κ light chains were used in all cases. **(f)** Heatmap of differentially expressed genes in IL6Myc-dependent PCT (*n* = 11) compared with normal B cells. Up- and down-regulated genes are indicated by red and blue, respectively. All tumor samples were obtained from enlarged MLNs. B cells were isolated from the spleens of 5-month-old C mice using B220 magnetic columns (Milteny, Auburn, CA, USA). The B220⁺ splenocytes were either left untreated (*n* = 3) or activated by treatment with lipopolysaccharide (LPS) and IL-4 (*n* = 3). Illumina microarray data were processed using GenomeStudio v1.9.0 (Illumina). Raw expression values were normalized using the quantile method and assessed for genes with differential expression based on analysis of variance (ANOVA). Probeset values were normalized to a mean of zero (that is, mean centered) and a s.d. of 1. The false discovery rate (FDR) was then applied to adjust *P*-values for multiple test correction. Differentially expressed genes were selected with thresholds based on FDR-adjusted *P*-value < 0.05 and fold change > 1.5 or < -1.5. **(g)** Shown to the left is a PCA (principal component analysis) plot of global gene expression of the tumor and control samples included in the heatmap presented above: A, quiescent B cells; B, proliferating B cells; C, PCT. Shown to the right is a Venn diagram that depicts the number of gene probes found to be significantly variable by ANOVA in pairwise comparisons using a cut-off threshold of FDR 0.05 and a fold expression change that is either > 1.5 or < -1.5. The 831 gene probes intersecting all four comparison groups are included in the heatmap in **(a)**. **(h)** Diagram showing expression levels of six genes found to be up- or down-regulated in PCT (*n* = 11) compared with normal B cells (*n* = 3 + 3). Mean gene expression levels (columns) and s.d. of the mean (vertical lines) are plotted. All differences between PCT and either unstimulated or stimulated B cells were significant (*P* < 0.05) using Student's *t*-test. **(i)** Infiltration of the bone marrow with malignant PCs. The left top panel depicts flow data on the presence of malignant, high forward scatter-gated CD138⁺ B220⁻ PCs (10.8%) in the femur of a C.IL6Myc mouse harboring a mid-stage PCT. B220 and CD138 were detected using phycoerythrin- and allophycocyanin-conjugated antibodies 6B2 (eBioscience, San Diego, CA, USA) and 281-2 (BD Biosciences, San Jose, CA, USA), respectively. Shown in the right top and bottom panels is a tissue section of a skull base bone of another mouse bearing a late-stage PCT. The normal marrow has been replaced entirely with malignant PCs (H&E; original magnification × 2 and × 63, respectively).

12h but had free access to water. Following determination of body weights (23.0 ± 5.30 g on average) and blood glucose levels (63.6 ± 21.2 mg/dl; Freestyle glucometer, Abbott Labs, Abbott Park, IL, USA), mice were anesthetized using vaporized isoflurane (4% for induction; 2.5% for maintenance). Sterile normal saline (0.1 ml) was injected subcutaneously to ensure adequate hydration. Following administration of ^{18}F -FDG (8.65 ± 2.7 MBq) via lateral tail vein injection, mice were

awakened and returned to individual holding cages. Precisely 60 min post FDG injection, re-anesthetized mice were placed prone in a heated (36°C) multimodality chamber (M2M Imaging, Cleveland, OH, USA) in the PET scanner's gantry. PET list mode data were acquired for 15 min, using an Inveon small-animal PET/CT/SPECT imaging system (Preclinical Solutions, Siemens Healthcare Molecular Imaging, Knoxville, TN, USA). In the same workflow, a CT image was acquired for attenuation correction purposes.



Images were reconstructed using a three-dimensional OP-MAP algorithm (Siemens Medical Solutions USA, Inc., Malvern, PA, USA). Scanner reconstructions using this algorithm were calibrated back to a National Institute of Standards and Technology (NIST)-traceable positron-emitting dose calibrator source to assure quantitative accuracy.

FDG-PET image analysis

Images were analyzed using PMOD v3.2 software (PMOD Technologies, Zurich, Switzerland). To determine tumor activity based on ^{18}F -FDG uptake in individual lesions, volumes of interest (VOIs) were drawn at sites known to display accumulation of aberrant PCs, particularly lymph nodes and spleen. A threshold algorithm (50% max–min) was applied to all detectable lesion sites for adequate volume contouring. The mean standardized uptake value (SUV_{mean}), maximal SUV (SUV_{max}), metabolic tumor volume ($\text{Vol}_{\text{metab}}$) and total lesion glycolysis ($\text{TLG} = \text{SUV}_{\text{mean}} \times \text{Vol}_{\text{metab}}$) were determined. SUV_{max} and $\text{Vol}_{\text{metab}}$ were used to assess tumor activity and growth, respectively. Means were calculated for the different parameters, expressed graphically and considered significantly different at two-tailed P -values of ≤ 0.05 . To better appreciate tumor contours in anatomical context, three-dimensional reconstruction of PET and CT modalities were generated using independent software (Inveon Research Workplace, Siemens Medical Solutions USA, Inc.).

Histopathology

C.iL6Myc mice were killed at early-, intermediate- and late-disease stages (47–51, 92–104 and 136–139 days, respectively) and a standard panel of tissues, including bones (skull, humerus, femur, vertebrae, sternum), lymphoid organs (lymph nodes, spleen) and parenchymatous organs (liver, kidney), was harvested, fixed in formalin and embedded in paraffin. Tissue sections (4 μm) were stained with hematoxylin and eosin and quantified for numbers of aberrant PCs in 10 different fields of view, using an Olympus (Center Valley, PA, USA) BX-61 light microscope and a 40x objective. Aberrant iL6Myc DTg PCs are larger than their normal counterparts, usually hyperchromatic, and sometimes mitotically active. Tissue infiltration with aberrant PCs was estimated using a scoring system with scores 0–4 denoting absence (0), $\leq 10\%$ (1), 10–49% (2), 50–79% (3) and $>80\%$ PCs (4), respectively.

RESULTS

Widespread Tg expression of IL-6 cooperates with deregulated Myc in B cells to drive PCT development in BALB/c mice

To determine whether the newly developed iMyc allele, $\text{iMyc}^{\Delta\text{E}\mu}$ (Figure 1a), would act synergistically with widespread Tg expression of IL-6 to promote malignant PC transformation in BALB/c (C) mice, homozygous Tg C.iMyc $^{\Delta\text{E}\mu}$ mice were crossed with heterozygous Tg C.iL6 mice to generate heterozygous DTg C.iL6Myc mice (Figure 1b). Fourteen DTg mice were monitored at

weekly intervals for signs of tumor development manifested by splenomegaly, generalized lymphadenopathy and/or hind leg paralysis (Figure 1c). All 14 mice exhibited signs of incipient neoplasia before 130 days of age, indicating complete genetic penetrance of the iL6Myc-driven phenotype. Median age of tumor onset was 106 days with a mean and s.d. of the mean of 96.1 ± 21.0 days and a range of 45–175 days. Tumor diagnosis was confirmed by histological studies of tissues obtained at necropsy. In all 14 cases, the tumors were positive for homogeneous sheets

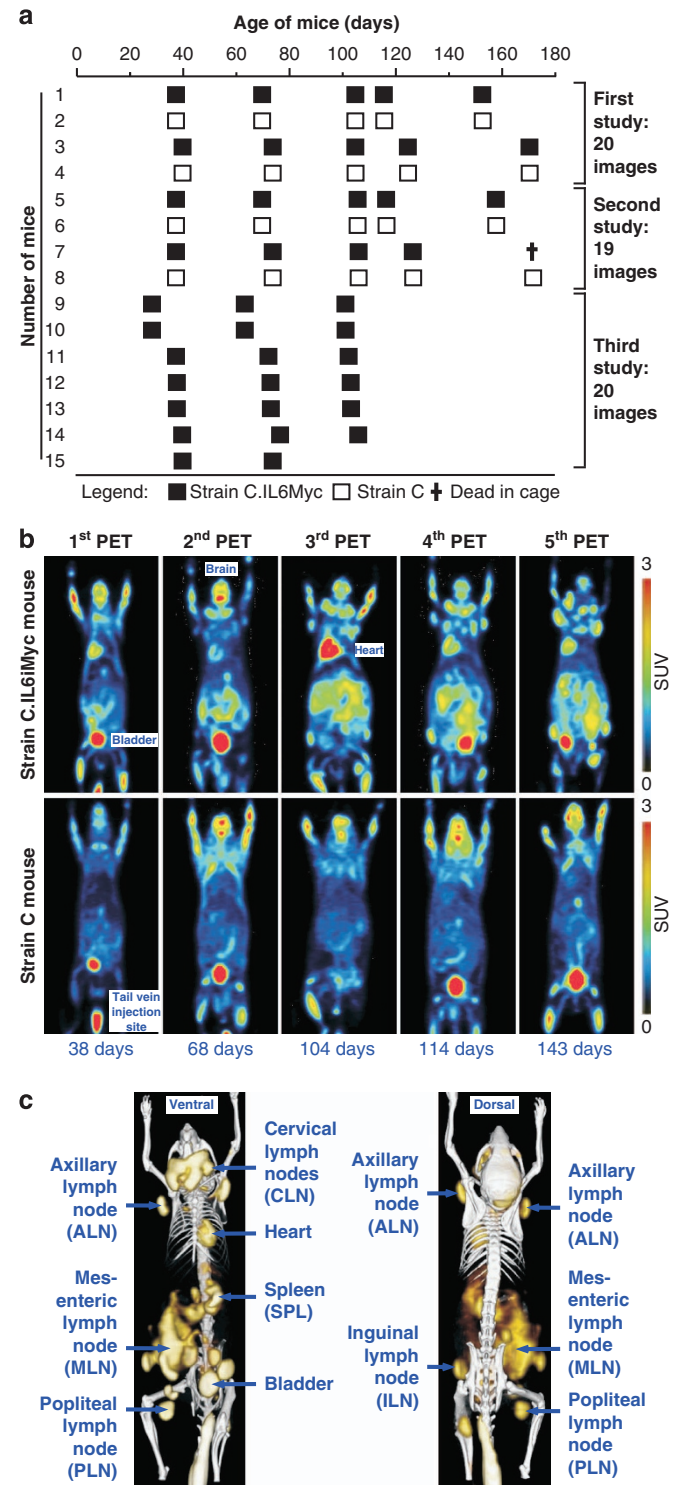


Figure 2. Monitoring PCT progression in individual C.iL6Myc mice using integrated FDG-PET and CT imaging. **(a)** FDG-PET imaging schedule of C.iL6Myc mice undergoing PCT development. The study included 11 Tg mice (black squares) and 4 normal C mice used as controls (open squares). The numbers of mice (displayed vertically) and ages of mice at time of PET scanning (displayed horizontally) are indicated. **(b)** Serial coronal PET images of a representative iL6Myc mouse (top) and a normal control (bottom) acquired between 38 and 143 days of age. All images were normalized to the same maximal standard uptake value ($\text{SUV}_{\text{max}} = 3$) to facilitate comparison of PET lesions. The steady increase in FDG uptake in peripheral and abdominal lymph nodes of the transgenic mouse (top panels) indicates the steady progression of PCT over time. High normal FDG uptake (not associated with tumor development) resulting in high PET signal strength is seen in brain and heart (tissues with physiologically high levels of glucose utilization), the FDG excretion pathway (urinary bladder and, to a lesser extent, kidneys) and the FDG injection site (lateral tail vein)—all readily detected in the normal mouse shown at the bottom. **(c)** Three-dimensional renderings of fused PET/CT images of the iL6Myc mouse from **(a)**. Integrated images of this sort facilitate the determination of tumor dissemination patterns and the precise anatomic localization of bone cavities containing PCT-laden hematopoietic marrow.

of clg⁺ PCs containing varying amounts of cytoplasm and eccentric nuclei with prominent nucleoli. Based on these features, the tumors were classified as PCTs (Figure 1d). Compared with DTg mice, tumor development in the single Tg counterparts was significantly slower: 8 C.iMyc mice developed tumors by 410 days of age (median: 251 days; mean: 269 ± 64.3 days; range: 213–410 days), a significant delay relative to strain C.iL6Myc by two-tailed *t*-test analysis ($P < 10^{-3}$). Similarly, as reported previously, C.iL-6 mice developed no more than 40% PCT by 12 months of age.²³ These findings underlined the striking efficiency with which IL-6 and Myc collaborate in PCT formation in strain C mice.³⁴

IL6Myc-driven PCTs recapitulate key features of human MM

Tumor-bearing C.iL6Myc mice exhibited paraprotein 'M-spikes' upon serum protein electrophoresis (Figure 1e), indicating either the presence of a single, greatly expanded clone of Ig-producing PCs (see, for example, the pronounced extragradient in lane 4) or the coexistence of two or more malignant cell clones prior to the emergence of the dominant clone (lanes 2, 5 and 8). Intraperitoneal injection of ~10⁶ putative tumor cells to pristane-primed normal C mice resulted uniformly in the outgrowth of a PCT that produced the same clonotypic M-spike (indicated by the same electrophoretic mobility) previously found in the donor mouse (not shown). This not only demonstrated that the aberrant PCs had completed malignant transformation, but also showed that immunoglobulin (Ig) expression is a reliable serum biomarker of IL6Myc-dependent tumors. Microarray-based global gene expression profiling demonstrated that PCT exhibited a characteristic gene expression profile distinct from that of normal untreated quiescent or activated proliferating B cells (Figure 1f). Principal component analysis of transcripts confirmed the tight clustering of tumor samples ($n = 11$) versus B-cell samples (Figure 1g, left). At a false discovery rate of <0.05, analysis of variance revealed 5047 and 2210 Illumina probesets that showed significant differences between PCT and quiescent and proliferating B cells, respectively (Figure 1g, right). PCT-typical changes included upregulation of cancer-associated genes such as *Plk3cg*, *S100a6* and *Vegfa*, and downregulation of B-cell genes such as *Bcl6*, *Cd19* and *Faim3* (Figure 1h). A remarkable feature of tumor-bearing C.iL6Myc mice was the infiltration of the bone marrow with malignant PCs as determined by flow cytometry. Figure 1i depicts the pathological accumulation of aberrant CD138⁺B220⁻ PCs in the femur of one

mouse containing an intermediate-stage PCT (top left) and the complete replacement of the normal marrow by a wall-to-wall infiltrate of malignant PCs in the base of the skull of another mouse with terminal disease (top right and bottom). Micro-CT analysis produced evidence for profound generalized and focal bone loss, including osteolytic lesions in long bones (Supplementary Movies) and separation of cranial sutures as recently seen in Bcl-X_LMyc mice,³⁸ indicating that C.iL6Myc mice are prone to MM-like bone disease. These results shall be reported in greater depth in a subsequent paper. These findings demonstrated the promise of strain C.iL6Myc for preclinical studies on human MM.

IL6Myc-driven PCTs are readily imaged using FDG-PET

To evaluate the feasibility of employing FDG-PET for the study of tumor progression in strain C.iL6Myc mice, we performed serial whole-body imaging of two pairs of age-matched Tg and control

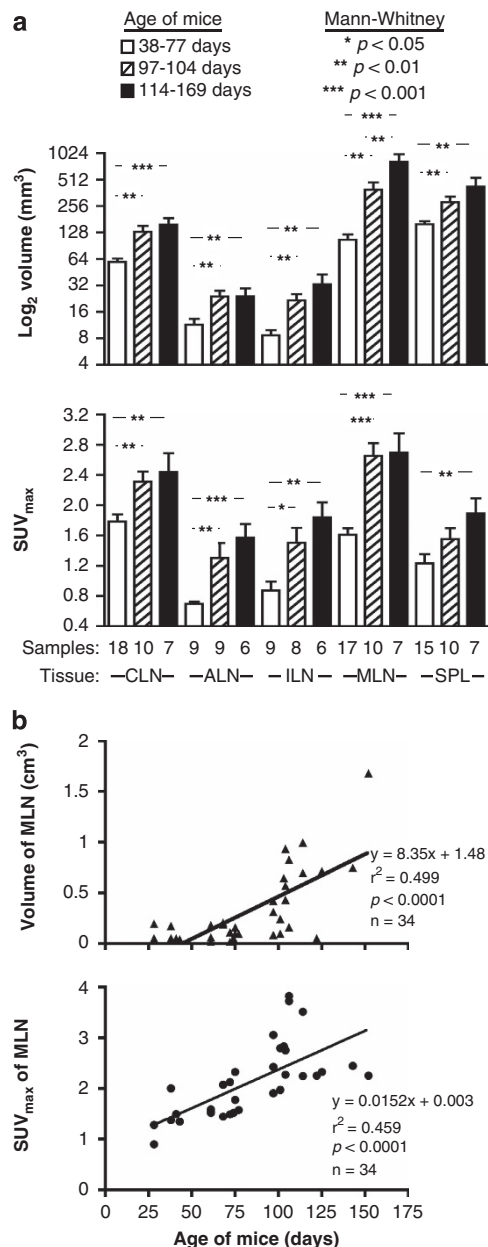


Figure 3. Increased FDG uptake rates in lymphoid tissues of C.iL6Myc mice undergoing PCT development. **(a)** Elevated metabolic activity in three different stages of tumor progression. Included in the analysis were CLN, ALN, (ILN and MLN as well as SPL. Ages of mice, which correspond to early (white), mid (hatched) and late (black) stages of tumor progression, are indicated at the top left. The number of tissue samples is indicated at the bottom. Regions of interest defined on PET images were placed in areas of focal FDG uptake not explained by the physiologic distribution and excretion of FDG. In cases where the identification of the underlying tissue was not straightforward, these regions were put in anatomical context using fused PET/CT images. Metabolic tissue volumes, Vol_{metab} (top) and maximal standardized uptake values, SUV_{max} (bottom), were calculated and mean values were compared using the two-tailed Mann-Whitney test. Significant differences between stages of tumor progression (two-tailed Mann-Whitney test) are indicated as * $P < 0.05$, ** $P < 0.01$ and *** $P < 0.001$. **(b)** FDG uptake in MLN is correlated with age of mouse. Vol_{metab} (top) and SUV_{max} (bottom) were obtained from 34 PET scans of all Tg mice included in Figure 3 ($n = 11$). Correlation parameters including linear regression coefficients (r^2) and significance values (P) are indicated. Supplementary Figure 2 presents SUV_{mean} and TLG data on MLN and Supplementary Figure 3 shows complete results (volume, SUV_{max}, SUV_{mean}, TLG) on all other lymphoid tissues included here (CLN, ALN, ILN and SPL).

normal mice (Figure 2a, first study). PET imaging began at an early 'pre-malignant' stage of tumor development (day 38 and 41 for mice 1 and 3, respectively) and ended at the stage of terminal disease that required killing humane reasons shortly after the final PET scan (day 143 and 169 for mice 1 and 3, respectively). Spaced in between the first and last scans, mice were imaged 3 more times; on days 68, 104 and 114 for mice 1 and 2 and on days 75, 104 and 125 for mice 3 and 4. The complete series of FDG-PET images of C.IL6Myc mouse 1 is presented in Figure 2b (top); the corresponding age-matched non-Tg control 2 is shown at the bottom). Changes very similar to those seen in mouse 1 were seen in mouse 3 (Supplementary Figure 1, left). End-stage whole-body tumor burden was visualized in three-dimensional renderings of the final FDG-PET/CT scan, represented by two different views of mouse 1 in Figure 2c. Essentially, identical changes were found in mouse 3 (Supplementary Figure 1, right). Necropsies of mice 1 and 3 performed immediately after the final imaging sessions revealed gross pathological findings similar to those presented in Figure 1c, and subsequent histopathological studies confirmed the diagnosis of PCT. These results provided strong suggestive evidence that integrated FDG-PET/CT imaging is a quality research tool for assessing spontaneously arising PCT in strain C.IL6Myc mice.

FDG-PET distinguishes early, intermediate and late stages of IL6/MYC-driven PCT

The reproducibility of the studies described above was assessed using the same PET schedule and two newly bred Tg mice 5 and 7 and age-matched controls 6 and 8 (Figure 2a, second study). Base FDG uptake of mouse 5 was measured at 38 days of age and tumor-dependent increases in metabolic activity were determined on days 68, 104, 114 and 152 (Supplementary Figure 1). Mouse 7 was imaged four times (days 38, 72, 101 and 122). The results of study 2, which generated 19 PET scans, largely confirmed the findings from the first study involving 20 scans, and also revealed difficulties in evaluating early stages of tumor progression in a fully reproducible and accurate manner. To address this problem and increase the PET data set of early IL6Myc-dependent changes, 7 additional Tg mice were imaged either thrice (9–14) or twice (15), at approximately monthly intervals between 28 and 106 days of age (Figure 2a, third study). Normal C mice were no longer included because the four controls from studies 1 and 2 demonstrated baseline levels of FDG uptake at all time points. Evaluation of the newly generated images from study 3 ($n=20$) permitted not only the detection of early stages of tumor development with greater confidence, and also led to the operational division of IL6Myc-driven PCT development into early (≤ 76 days of age), intermediate (77–104 days) and late stages (> 104 days) of tumor development. These stages will be used hereafter to quantitatively describe PCT progression using PET-derived parameters.

FDG-PET parameters permit quantitative analysis of PCT progression

The 39 serial FDG-PET scans of C.IL6Myc mice from studies 1 to 3 were analyzed in a standardized manner that relies on the algorithms described in the Methods section. VOIs were drawn in areas of focal FDG uptake to first determine tissue/lesion size (Figure 3a, top) and then estimate metabolic activity using the SUV_{max} (Figure 3a, bottom). The top panel of Figure 5 depicts the steady increase in mean volume of lymphoid tissues in the course of tumor progression, employing (1) three different peripheral lymph nodes (cervical (CLN), axillary (ALN) and inguinal (ILN)), (2) the assembly of 6–8 deep abdominal lymph nodes commonly referred to as the mesenteric node (MLN) and (3) the spleen (SPL). Volume increases varied considerably among tissues, ranging from 2.1-fold in case of ALN (11.5 mm^3 at early stage of tumor development versus 24 mm^3 at late stage) to 7.7-fold in case of

MLN (106 vs 817 mm^3). Elevations in SUV_{max} showed markedly less variation in comparisons among sites, indicated by a 1.37-fold increase (1.78–2.26) in CLN and a 2.26-fold increase (0.695–1.57) in ALN. These defined the minimal and maximal changes, respectively. Increases in mean SUV (SUV_{mean}) were similarly consistent among all tissues (Supplementary Figure 2, top). Next, the tissue volume was multiplied by the SUV_{mean} to estimate the TLG, a parameter that represents the total metabolic activity of each lesion. The bottom panel of Supplementary Figure 2 shows that tumor progression in IL6Myc-Tg mice was accompanied by a significant increase in TLG in all tissues. Unsurprisingly, if one considers its large increase in size during tumor development, the MLN exhibited the highest increase in TLG (12.7-fold). This was followed by ILN (6.12-fold), ALN (5.03-fold), SPL (4.11-fold) and CLN (3.81-fold). Linear regression analysis of PET image-derived measurements of VOI, SUV_{max} , SUV_{mean} and TLG in the Tg mice uniformly demonstrated a significant correlation among PET parameters with age (Supplementary Figure 3). This not only

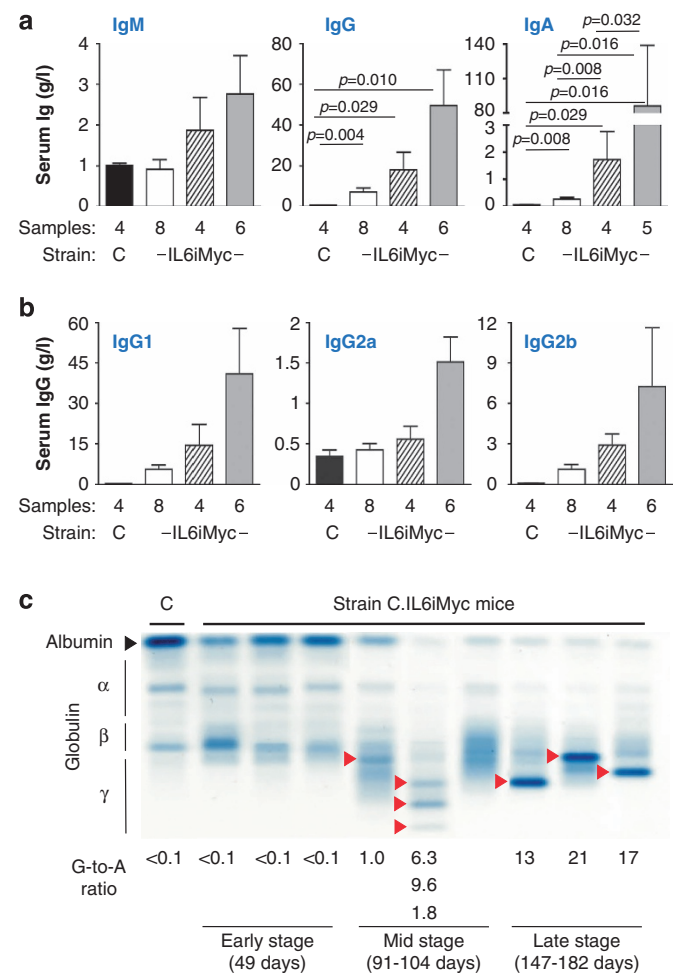


Figure 4. Increase in serum Ig levels and emergence of serum paraproteins in the course of PCT development. **(a, b)** Serum Ig levels were determined using isotype-specific enzyme-linked immunosorbent assay (ELISA). Normal C mice (black) were compared with IL6Myc-Tg mice at early (white columns), mid (hatched) and late (grey) stages of tumor progression as defined in Figure 5a. Statistical comparisons of stages of tumor progression were carried out using the two-tailed *t*-test; *P*-values are indicated where the threshold of significance (5%) was reached. **(c)** Paraproteins (indicated by red arrowheads) were detected using serum protein electrophoresis. Age of mice and ratio of γ -globulins to albumin (G/A) are indicated at the bottom.

strengthened the rationale for defining the three stages of tumor progression, but also suggested that PCT development is a continuous process during which tumor cells gradually increase metabolic activity while accumulating in lymphoid tissues. In agreement with the results presented in Figures 2b and c and Supplementary Figure 1, the MLN exhibited the steepest slope in all regression curves, indicating that tumor-dependent changes in VOI and SUV_{max} (Figure 3b) and SUV_{mean} and TLG (Supplementary Figures 2 and 3) occur in this tissue site with maximum velocity. These findings provided further evidence for the usefulness of FDG-PET in assessing IL6Myc-driven tumor progression in a reproducible, objective manner.

Serum Ig and histopathologic analyses of PCT-bearing mice validate FDG-PET results

Because serum Ig levels are a well-established molecular biomarker of MM and related B-lineage neoplasms, serum Ig levels were determined by enzyme-linked immunosorbent assay. Figure 4a depicts the steady increase in the three main classes of serum Ig in the course of IL6Myc-dependent tumor progression. Compared with normal mice, Tg mice with late stage of disease exhibited a modest 3-fold increase in IgM levels, a marked 87-fold increase in IgG levels and a striking ~1400-fold increase in IgA levels. In agreement with the known predilection of B cells from IL-6 Tg mice to produce IgG1,⁴³ the increase in the levels of this isotype was greater (155-fold) than that of IgG2b (~84-fold) and IgG2a (~3-fold, Figure 4b). Serum protein electropherograms of three representative Tg mice at early, mid and late stages of tumor development helped to visualize the progressive hyperimmunoglobulinemia, inevitably resulting in the emergence of M-spikes in mice harboring incipient tumors (Figure 4c). Histopathologic analysis of tissue sections was next performed to validate PET-

derived results on PCT progression using an independent method. The analysis revealed the steady accumulation of aberrant PCs in tissues, first noted in lymph nodes and spleen, then in the bone marrow, and finally in nonlymphoid tissues such as liver and kidney (Figure 5). These findings demonstrated that tumor progression changes detected by FDG-PET in C.IL6Myc mice are tightly correlated with increased Ig production and a vast expansion of the total PC compartment, strongly supporting the underlying rationale for the PET-based, lesion-specific staging system of IL6Myc-dependent PCT presented in Supplementary Figure 4.

FDG-PET enables assessment of objective treatment responses to proteasome inhibitor ixazomib

To test the possibility that FDG-PET gives us the means to assess objective myeloma drug responses in PCT-bearing mice in a preclinical setting, a small pilot study using six mice treated with the investigational proteasome inhibitor ixazomib (Millennium Pharmaceuticals, Inc., Cambridge, MA, USA)^{37,44,45} was performed (Figure 6a). Following imaging-based tumor diagnosis at 97–106 days of age, the mice were treated with bi-weekly intravenous injections of 7mg/kg ixazomib—a dose shown to be well tolerated and effective in a recent study on PCT inhibition in Bcl-X_LMyc mice.³⁸ Follow-up PET scans demonstrated that ixazomib was remarkably active in 5 of 6 mice (16–20, Figure 6b), extending overall survival by 91.6 days on average (range 54–176 days). This corresponded to a near doubling of the mean life expectancy of treated mice (187.6 days) compared with untreated controls (96.1 days). The striking reduction in tumor burden after only three administrations of drug in one representative case (mouse 17) underscored the activity of ixazomib in IL6Myc mice (Figure 6c). Drug-induced tumor remission was deep

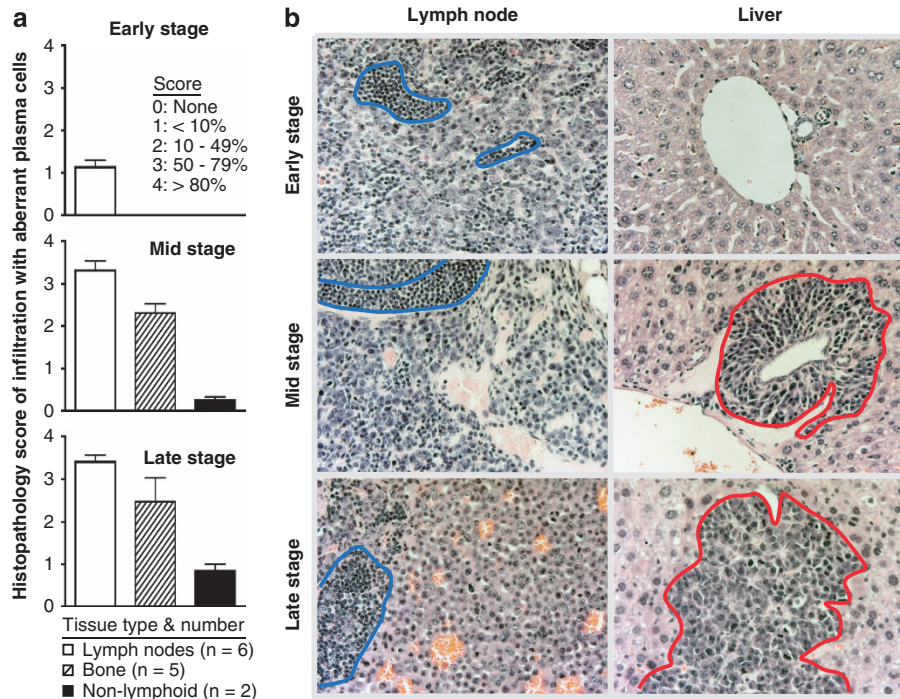


Figure 5. Increasing abundance of aberrant plasma cells in the course of IL6Myc-driven tumor formation. **(a)** Mean histopathology scores of tissue infiltration with abnormal PCs at early (top), mid (center) and late (bottom) stages of PCT development as defined in the top panel. The scoring system distinguishes lack of such PCs (0), presence of <50% (1) or <80% (2) of PCs, >80% (3), and complete effacement of normal histology by PCT (4). **(b)** Representative hematoxylin and eosin (H&E)-stained tissue sections of secondary lymphoid tissues (lymph nodes, left) and nonlymphoid tissues (liver sections, right) at early (top), mid (center) and late (bottom) stages of PCT development. In the lymph node images, aggregates of normal lymphocytes are circled in blue to facilitate comparison with aberrant PCs. Plasmacytic infiltrates in liver (that is, portal pattern in the mid-stage example and interstitial pattern in the late-stage example) are circled in red.

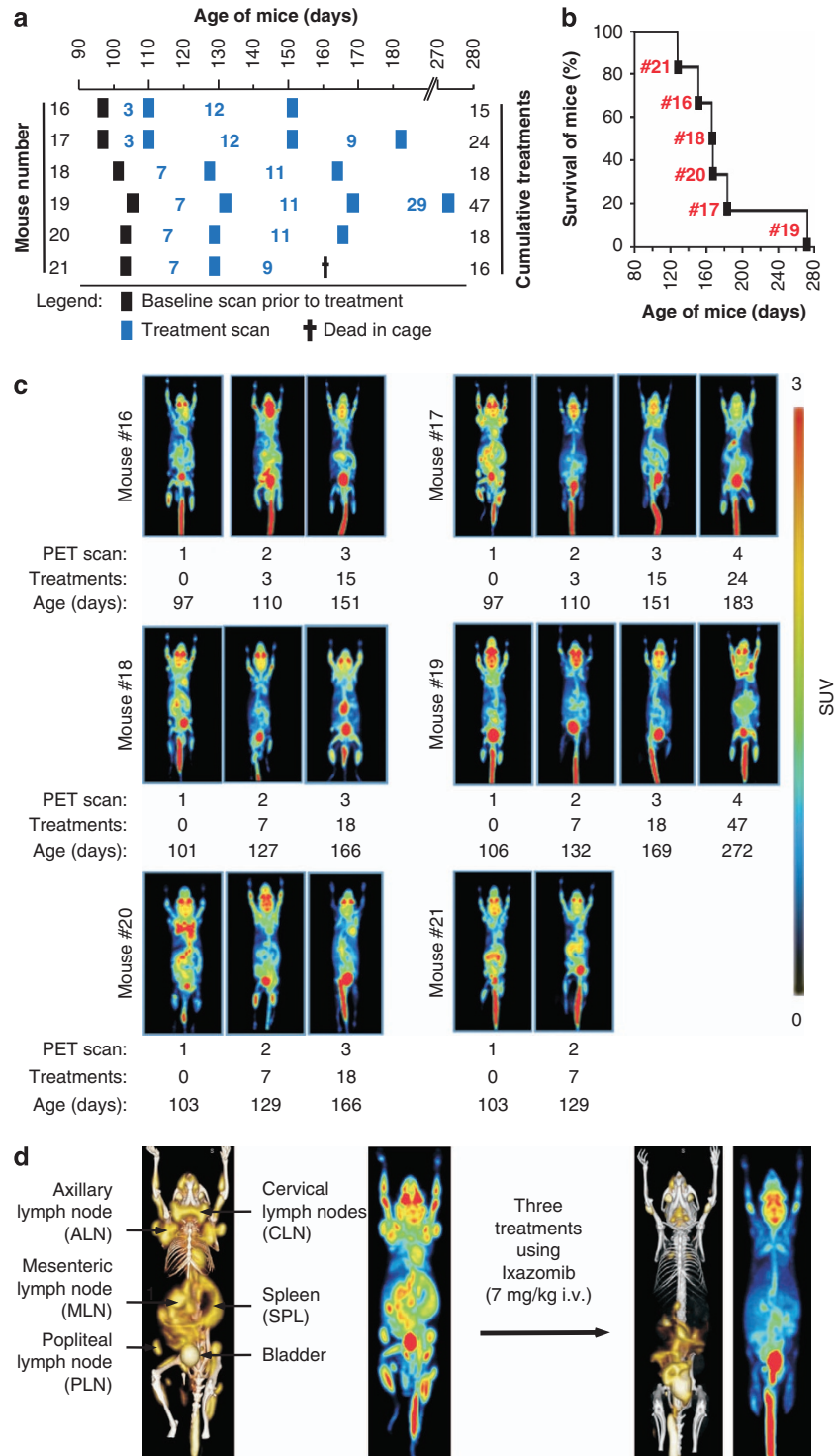


Figure 6. Assessing objective responses of PCT-bearing C.IL6Myc mice to treatment with the next-generation proteasome inhibitor, ixazomib. **(a)** FDG-PET imaging schedule of tumor-bearing mice ($n=6$) undergoing treatment with ixazomib. PET scans at baseline before commencement of therapy are indicated by black squares. Treatment scans are depicted by blue squares. The number of drug applications between PET scans is indicated in blue; the cumulative, total number is indicated vertically on the right. Mouse age and number are displayed horizontally and vertically on the left, respectively. Ixazomib was dissolved in 5% hydroxypropyl- β -cyclodextrin (5% HP β CD) and administered in the lateral tail vein at 7 mg/kg body weight. Mouse 21 was found dead in cage just before the scheduled second treatment scan (black cross symbol). **(b)** Kaplan–Meier curve demonstrating survival of ixazomib-treated mice included in **(a)**. Mouse numbers are indicated in red. **(c)** Serial coronal maximal projection PET images of mice treated with ixazomib. All images were normalized to a SUV_{max} of 3. Mice 16–20 achieved tumor remission upon treatment with drug, but mouse 21 had refractory disease. **(d)** Three-dimensional renderings of integrated PET/CT images of an IL6Myc mouse that has received four treatments with ixazomib. Decreases in FDG uptake in peripheral and abdominal lymph nodes reflect response to treatment, whereas increases indicate tumor relapse.

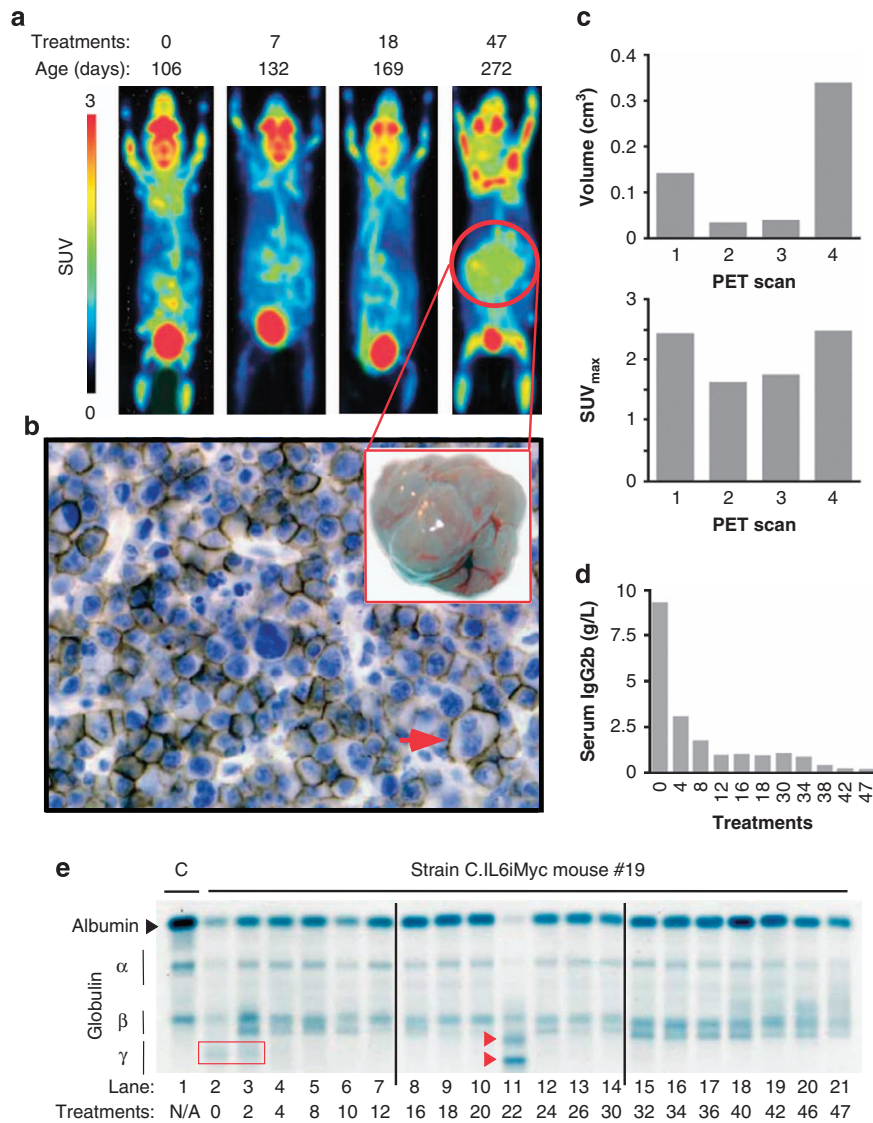


Figure 7. Durable remission followed by an apparent single-site relapse in a PCT-bearing mouse treated for 24 weeks with ixazomib. **(a)** Serial coronal FDG-PET images demonstrating local tumor relapse in mouse 19 after 47 treatments with ixazomib. Shown are (1) a baseline image before commencement of therapy at 106 days of age (left panel), (2) two PET images during tumor remission after 7 and 18 administrations of drug (middle panels) and (3) a terminal PET image that shows massive tumor relapse in the abdominal cavity (red circle) after 47 drug treatments. Necropsy revealed a round, solitary abdominal tumor (diameter ~1.5 cm) that most likely originated in the MLN. The terminal PET scan also indicates increased metabolic activity in the hematopoietic bone marrow of both forelimbs. All PET images were normalized to SUV_{max} of 3. **(b)** Gross pathology (inset) and histopathology of tumor relapse. Tumor tissue was fixed in formalin, embedded in paraffin, sectioned at 4 μ m, immunolabeled with antibody to CD138 and counterstained with hematoxylin. Surface expression of CD138 (brown staining of cell membranes) and cytological features of tumor cells (including occurrence of large, bi- and multinucleated plasma cells like the one indicated by red arrow) were consistent with the diagnosis of anaplastic plasmacytoma. **(c)** Image-derived parameters of tumor regression and relapse. Metabolic tissue volumes (top) and maximal standardized uptake values (bottom) were calculated for each PET scan and used as indicators of metabolic activity of the MLN tumor. The metabolic volume exhibited greater changes (~6-fold drop during remission (scans 2 and 3) and ~2.5-fold increase at relapse (scan 4) compared with baseline) than SUV_{max} (~25% reduction during remission and return to baseline at relapse). **(d)** Treatment-dependent decrease of serum IgG2b levels as determined by isotype-specific enzyme-linked immunosorbent assay (ELISA). The reference value for normal age-matched C mice is ≤ 0.1 g/l. The peak value of ~9 g/l at baseline agreed with the detection of an IgG2b paraprotein using serum protein electrophoresis ((e), lanes 2 and 3). **(e)** Serial serum protein electropherograms (three different gels) demonstrating the swift disappearance of the relatively small IgG2b paraprotein (lanes 2 and 3) upon treatment with ixazomib. Two relatively strong but transitory M-spikes (lane 11) that popped up after 22 administrations of drug (red arrowheads) but had vanished on week later (lane 12) were likely unrelated to the tumor relapse, but this was not shown. Lane 1 contains a serum sample from an age-matched normal C mouse that was used as control.

in all five responders, but the duration of the response was variable (range 55–176 days). The most profound and sustained remission, which lasted for almost 6 months of continuous twice-weekly treatment, is described in greater detail in Figure 7. In this case, image-derived parameters, serum IgG2b levels and serum protein electrophoresis all detected the response to treatment,

but only the imaging method detected the relapse. One mouse (21), an apparent outlier with regard to drug sensitivity, did not respond to ixazomib, suggesting primary refractory disease (Figure 8). The underlying reason, for example, drug-resistant PCT versus disease heterogeneity in C.I.L6Myc mice resulting in neoplasms other than PCT, remained unknown. These results

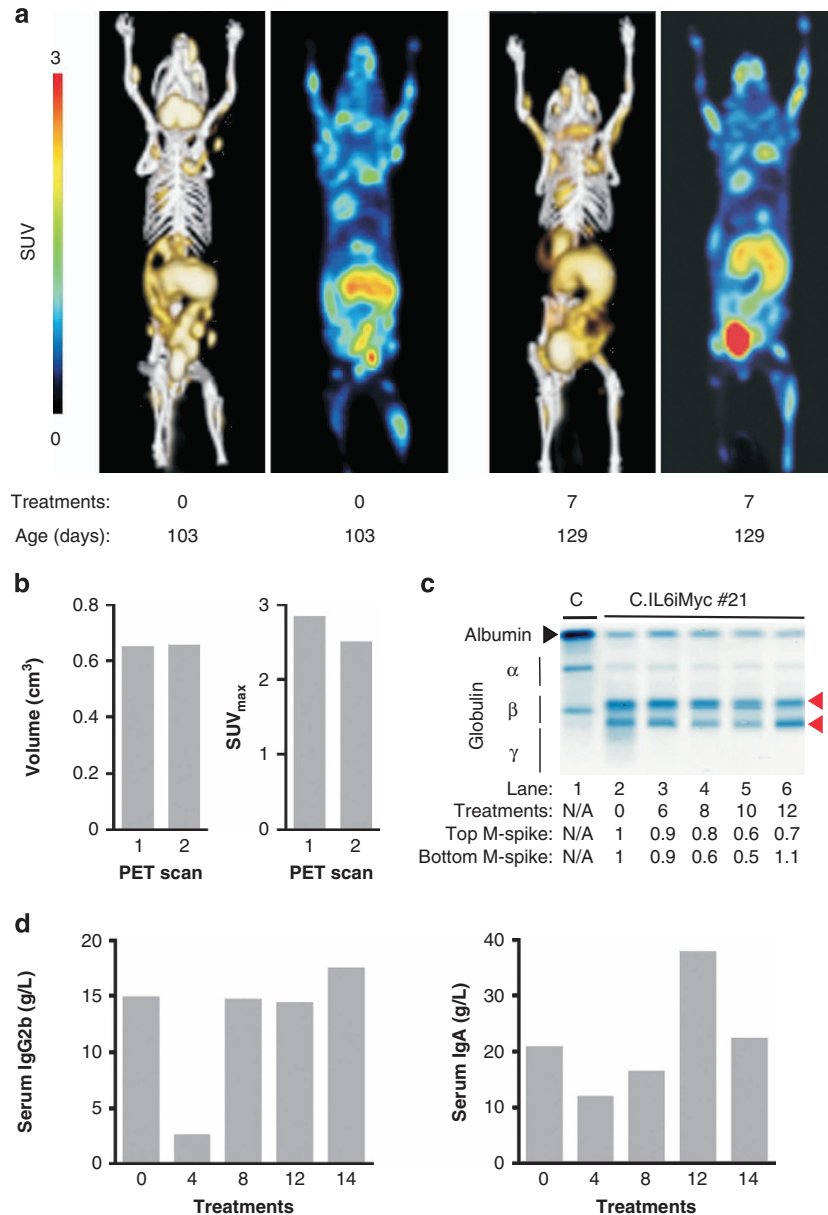


Figure 8. Primary refractory disease in a PCT-bearing C.I.L6Myc mouse treated with ixazomib. **(a)** FDG-PET images demonstrating the nonresponsiveness of mouse 21 to treatment with ixazomib. Paired coronal and 3D PET images at baseline (left) and after 7 administrations of drug (right) are shown. Both PET images were normalized to SUV_{max} of 3. **(b)** Image-derived parameters of refractory neoplasia. Metabolic tissue volumes (left) and maximal standardized uptake values (right) were calculated for both PET scans and used as indicators of metabolic activity of the abdominal tumor mass. There was essentially no change in both parameters, indicating lack of therapeutic benefit. **(c)** Serum protein electropherograms showing that M-spikes persist upon treatment with ixazomib. The two paraproteins found in this mouse were isotyped as IgG2b and IgA. Their abundance upon treatment of the mouse (lanes 3–6) relative to baseline before treatment (lane 2) is indicated at the bottom. The mouse was kept alive for 9 additional treatments after the second PET scan (which occurred after 7 treatments as indicated in **(a)**) but was found dead in cage just before the scheduled third scan could be performed (see cross symbol in Figure 6a). **(d)** Isotype-specific enzyme-linked immunosorbent assay (ELISA) results demonstrating persistent IgG2b (left) and IgA (right) paraproteins. The reference value of serum IgA for normal age-matched C mice is ≤ 0.01 g/L.

provided proof of principle that FDG-PET is suitable for measuring preclinical myeloma drug responses in a quantitative, reproducible and lesion-specific manner.

DISCUSSION

The main result of this study is the validation of FDG-PET as a preclinical research tool for assessing PCT progression and treatment responses in C.I.L6Myc mice—a strain of mice genetically predisposed to a type of PC neoplasia that recapitulates

several key features of human MM, including high-level production of paraproteins, changes in gene expression that are comparable to those seen in MM, infiltration of the bone marrow with malignant PCs and MM-like bone disease. The ability of FDG-PET to assess IL6Myc-driven tumor development in a serial, quantitative and stage-specific manner positions us to increase the value of strain C.I.L6Myc for basic and translational myeloma studies. For example, preclinical evaluation of new strategies for MM treatment and prevention will no longer be limited to the widely used but imprecise end points of tumor onset and tumor

incidence, but will also include tissue- and lesion-specific end points such as growth rate and metabolic activity of individual lymph nodes and relative tumor burden in medullary versus extramedullary tissue sites, as demonstrated in the studies described here with the proteasome inhibitor ixazomib. Use of these new end points is likely to increase the relevance of preclinical mouse MM-related studies and permit us to design preclinical co-trials of experimental MM drugs that mimic the circumstances of clinical trials more closely than possible in the past. The benefits of FDG-PET described above are not restricted to the C.I.L6Myc model of MM, but should apply more generally to many other mouse models of this common blood cancer.

The findings reported here extend previous work by other investigators who pioneered the application of FDG-PET for studies of *de novo* tumor development in Tg mouse models of human pancreatic cancer,⁴⁶ colon cancer⁴⁷ and thymoma,⁴⁸ and also encountered problems that limited the scope of their investigations. PET imaging in the pancreatic cancer model was limited to proof-of-principle in terms of tumor detection—no attempt was made to monitor tumor progression in individual mice in a quantitative, objective manner. In the colon cancer model, adenomas could only be visualized upon PET imaging *ex vivo*, as lesion-specific imaging *in vivo* was not feasible.⁴⁷ The study on thymomas was inadvertently handicapped by the anatomic location of the thymus in close proximity to the heart—a tissue with major physiologic uptake of FDG that tends to overwhelm the comparably small changes in metabolic activity (FDG uptake) of nearby tissues. The FDG-PET approach used in the present study has overcome the shortcomings noted above. Our results are reliable because the PET-based findings on PCT development were confirmed by serum biomarker analysis (serum Ig levels; detection of paraproteins) and histopathological findings (tumor progression score). Indeed, the convergence of image-dependent and -independent results supports the contention that FDG-PET imaging of IL6Myc-dependent tumors recapitulates many features of MM imaging, including tumor staging, in the clinic.

This study also has limitations that must be addressed in future work. Compared with the wealth and sophistication of imaging methods available for patients with MM, the sole reliance here on one method, FDG-PET, is a reminder that preclinical imaging of PCT in mice is in its infancy. In imaging MM, MRI supplements PET in more ways than one; for example, MRI is viewed by many as superior in detecting active MM,⁴⁹ and new modifications of MRI, such as diffusion-weighted and dynamic contrast-enhanced imaging,⁵⁰ promise further improvement in the near future. Inclusion of micro-MRI, which is available for small laboratory animal imaging, is therefore warranted for future imaging studies of C.I.L6Myc mice. Similarly, considering that CT is an established imaging method for assessing MM bone disease, micro-CT should be routinely included in future research on IL6Myc-dependent bone disease. Finally, with regard to PET tracers other than ¹⁸F-FDG, ¹⁸F-FLT (tracer of cell proliferation), ¹⁸F-NaF (tracer of bone formation) and ¹¹C-methionine (tracer of protein synthesis)⁵¹ all show potential for enhanced MM imaging in the clinic but have not been evaluated in mouse models of MM. Our preliminary experience with FLT in C.I.L6Myc mice resulted in disappointment thus far, agreeing with published findings on generally low uptake of FLT in mouse due to competition with high thymidine serum levels.⁵² Experiences of this sort suggest that it may be naive to expect that imaging modalities optimized for human MM can be readily adopted for preclinical MM imaging. Instead, additional research is warranted to work out optimal imaging protocols for mouse models of MM.

CONFLICT OF INTEREST

AJB is a current employee of Takeda Pharmaceutica Company Ltd (Cambridge, MA, USA). All other authors declare no conflict of interest.

ACKNOWLEDGEMENTS

This research was performed by KD in partial fulfillment of the requirements for the Degree Master of Sciences in the Graduate Program of the University of Iowa Department of Pathology. We thank Ling Hu for expert mouse husbandry. This work was supported in part by the Intramural Research Program of the NIAID (to HCM), by NCI core Grant P30CA086862 in support of The University of Iowa Holden Comprehensive Cancer Center (HCCC), by an Oberley Research Grant from HCCC (to JJS), by research awards from the Multiple Myeloma Research and International Waldenström's Macroglobulinemia Foundations (to SJ) and by R01CA151354 from the NCI (to SJ).

REFERENCES

- 1 Dimopoulos M, Terpos E, Comenzo RL, Tosi P, Beksac M, Sezer O *et al*. International myeloma working group consensus statement and guidelines regarding the current role of imaging techniques in the diagnosis and monitoring of multiple myeloma. *Leukemia* 2009; **23**: 1545–1556.
- 2 D'Sa S, Abildgaard N, Tighe J, Shaw P, Hall-Craggs M. Guidelines for the use of imaging in the management of myeloma. *Br J Haematol* 2007; **137**: 49–63.
- 3 Bredella MA, Steinbach L, Caputo G, Segall G, Hawkins R. Value of FDG PET in the assessment of patients with multiple myeloma. *AJR Am J Roentgenol* 2005; **184**: 1199–1204.
- 4 Mouloupos LA, Dimopoulos MA. Magnetic resonance imaging of the bone marrow in hematologic malignancies. *Blood* 1997; **90**: 2127–2147.
- 5 Balleari E, Villa G, Garre S, Ghirlanda P, Agnese G, Carletto M *et al*. Technetium-99m-sestamibi scintigraphy in multiple myeloma and related gammopathies: a useful tool for the identification and follow-up of myeloma bone disease. *Haematologica* 2001; **86**: 78–84.
- 6 Zamagni E, Cavo M. The role of imaging techniques in the management of multiple myeloma. *Br J Haematol* 2012; **159**: 499–513.
- 7 Bartel TB, Haessler J, Brown TL, Shaughnessy JD Jr, van Rhee F, Anaissie E *et al*. F18-fluorodeoxyglucose positron emission tomography in the context of other imaging techniques and prognostic factors in multiple myeloma. *Blood* 2009; **114**: 2068–2076.
- 8 Spinnato P, Bazzocchi A, Brioli A, Nanni C, Zamagni E, Albisinni U *et al*. Contrast enhanced MRI and (18)F-FDG PET-CT in the assessment of multiple myeloma: a comparison of results in different phases of the disease. *Eur J Radiol* 2012; **81**: 4013–4018.
- 9 Fletcher JW, Djulbegovic B, Soares HP, Siegel BA, Lowe VJ, Lyman GH *et al*. Recommendations on the use of 18F-FDG PET in oncology. *J Nucl Med* 2008; **49**: 480–508.
- 10 Kim JW, Dang CV. Cancer's molecular sweet tooth and the Warburg effect. *Cancer Res* 2006; **66**: 8927–8930.
- 11 Hanrahan CJ, Christensen CR, Crim JR. Current concepts in the evaluation of multiple myeloma with MR imaging and FDG PET/CT. *Radiographics* 2010; **30**: 127–142.
- 12 Nanni C, Rubello D, Zamagni E, Castellucci P, Ambrosini V, Montini G *et al*. 18F-FDG PET/CT in myeloma with presumed solitary plasmacytoma of bone. *In Vivo* 2008; **22**: 513–517.
- 13 van Lammeren-Venema D, Regelink JC, Riphagen II, Zweegman S, Hoekstra OS, Zijlstra JM. (1)(8)F-fluoro-deoxyglucose positron emission tomography in assessment of myeloma-related bone disease: a systematic review. *Cancer* 2012; **118**: 1971–1981.
- 14 Salaun PY, Gastinne T, Frampas E, Bodet-Milin C, Moreau P, Bodere-Kraeber F. FDG-positron-emission tomography for staging and therapeutic assessment in patients with plasmacytoma. *Haematologica* 2008; **93**: 1269–1271.
- 15 Elliott BM, Peti S, Osman K, Scigliano E, Lee D, Isola L *et al*. Combining FDG-PET/CT with laboratory data yields superior results for prediction of relapse in multiple myeloma. *Eur J Haematol* 2011; **86**: 289–298.
- 16 Walker RC, Brown TL, Jones-Jackson LB, De Blanche L, Bartel T. Imaging of multiple myeloma and related plasma cell dyscrasias. *J Nucl Med* 2012; **53**: 1091–1101.
- 17 Zamagni E, Patriarca F, Nanni C, Zannetti B, Englaro E, Pezzi A *et al*. Prognostic relevance of 18-F FDG PET/CT in newly diagnosed multiple myeloma patients treated with up-front autologous transplantation. *Blood* 2011; **118**: 5989–5995.
- 18 Potter M. Neoplastic development in plasma cells. *Immunol Rev* 2003; **194**: 177–195.
- 19 Chesi M, Robbani DF, Sebag M, Chng WJ, Affer M, Tiedemann R *et al*. AID-dependent activation of a MYC transgene induces multiple myeloma in a conditional mouse model of post-germinal center malignancies. *Cancer Cell* 2008; **13**: 167–180.
- 20 Carrasco DR, Sukhdeo K, Protopopova M, Sinha R, Enos M, Carrasco DE *et al*. The differentiation and stress response factor XBP-1 drives multiple myeloma pathogenesis. *Cancer Cell* 2007; **11**: 349–360.

- 21 Chiarle R, Gong JZ, Guasparri I, Pesci A, Cai J, Liu J *et al*. NPM-ALK transgenic mice spontaneously develop T-cell lymphomas and plasma cell tumors. *Blood* 2003; **101**: 1919–1927.
- 22 Silva S, Kovalchuk AL, Kim JS, Klein G, Janz S. BCL2 accelerates inflammation-induced BALB/c plasmacytomas and promotes novel tumors with coexisting T(12;15) and T(6;15) translocations. *Cancer Res* 2003; **63**: 8656–8663.
- 23 Kovalchuk AL, Kim JS, Park SS, Coleman AE, Ward JM, Morse 3rd HC *et al*. IL-6 transgenic mouse model for extramedullary plasmacytoma. *Proc Natl Acad Sci USA* 2002; **99**: 1509–1514.
- 24 Takizawa M, Tolarova H, Li Z, Dubois W, Lim S, Callen E *et al*. AID expression levels determine the extent of cMyc oncogenic translocations and the incidence of B cell tumor development. *J Exp Med* 2008; **205**: 1949–1957.
- 25 Linden M, Kirchhof N, Carlson C, Van Ness B. Targeted overexpression of Bcl-XL in B-lymphoid cells results in lymphoproliferative disease and plasma cell malignancies. *Blood* 2004; **103**: 2779–2786.
- 26 Vicente-Duenas C, Romero-Camarero I, Gonzalez-Herrero I, Alonso-Escudero E, Abollo-Jimenez F, Jiang X *et al*. A novel molecular mechanism involved in multiple myeloma development revealed by targeting MafB to haematopoietic progenitors. *EMBO J* 2012; **31**: 3704–3717.
- 27 Qi CF, Zhou JX, Lee CH, Naghashfar Z, Xiang S, Kovalchuk AL *et al*. Anaplastic, plasmablastic, and plasmacytic plasmacytomas of mice: relationships to human plasma cell neoplasms and late-stage differentiation of normal B cells. *Cancer Res* 2007; **67**: 2439–2447.
- 28 Rosenbaum H, Harris AW, Bath ML, McNeill J, Webb E, Adams JM *et al*. An E mu-v-abl transgene elicits plasmacytomas in concert with an activated myc gene. *EMBO J* 1990; **9**: 897–905.
- 29 Park SS, Kim JS, Tassarollo L, Owens JD, Peng L, Han SS *et al*. Insertion of c-Myc into Igh induces B-cell and plasma-cell neoplasms in mice. *Cancer Res* 2005; **65**: 1306–1315.
- 30 Truffinet V, Pinaud E, Cogne N, Petit B, Guglielmi L, Cogne M *et al*. The 3' IgH locus control region is sufficient to deregulate a c-myc transgene and promote mature B cell malignancies with a predominant Burkitt-like phenotype. *J Immunol* 2007; **179**: 6033–6042.
- 31 Gladden AB, Woolery R, Aggarwal P, Wasik MA, Diehl JA. Expression of constitutively nuclear cyclin D1 in murine lymphocytes induces B-cell lymphoma. *Oncogene* 2006; **25**: 998–1007.
- 32 Hartley JW, Chattopadhyay SK, Lander MR, Tadesse-Heath L, Naghashfar Z, Morse 3rd HC *et al*. Accelerated appearance of multiple B cell lymphoma types in NFS/N mice congenic for ecotropic murine leukemia viruses. *Lab Invest* 2000; **80**: 159–169.
- 33 Boylan KL, Gosse MA, Staggs SE, Janz S, Grindle S, Kansas GS *et al*. A transgenic mouse model of plasma cell malignancy shows phenotypic, cytogenetic, and gene expression heterogeneity similar to human multiple myeloma. *Cancer Res* 2007; **67**: 4069–4078.
- 34 Rutsch S, Neppalli VT, Shin DM, DuBois W, Morse 3rd HC, Goldschmidt H *et al*. IL-6 and MYC collaborate in plasma cell tumor formation in mice. *Blood* 2010; **115**: 1746–1754.
- 35 Janz S. Myc translocations in B cell and plasma cell neoplasms. *DNA Repair (Amst)* 2006; **5**: 1213–1224.
- 36 Kovalchuk AL, Kishimoto T, Janz S. Lymph nodes and Peyer's patches of IL-6 transgenic BALB/c mice harbor T(12;15) translocated plasma cells that contain illegitimate exchanges between the immunoglobulin heavy-chain mu locus and c-myc. *Leukemia* 2000; **14**: 1127–1135.
- 37 Chauhan D, Tian Z, Zhou B, Kuhn D, Orlowski R, Raju N *et al*. In vitro and in vivo selective antitumor activity of a novel orally bioavailable proteasome inhibitor MLN9708 against multiple myeloma cells. *Clin Cancer Res* 2011; **17**: 5311–5321.
- 38 Lee EC, Fitzgerald M, Bannerman B, Donelan J, Bano K, Terkelsen J *et al*. Antitumor activity of the investigational proteasome inhibitor MLN9708 in mouse models of B-cell and plasma cell malignancies. *Clin Cancer Res* 2011; **17**: 7313–7323.
- 39 Kumar SK, Berdeja RN, Niesvizky R, Lonial S, Hamadani M, Stewart AK *et al*. A phase 1/2 study of weekly MLN9708, an investigational oral proteasome inhibitor, in combination with lenalidomide and dexamethasone in patients with previously untreated multiple myeloma (MM). *Blood (ASH Annual Meeting Abstracts)* 2012; **120**: 332.
- 40 LeGrand J, Park ES, Wang H, Gupta S, Owens Jr. JD, Nelson PJ *et al*. Global gene expression profiling in mouse plasma cell tumor precursor and bystander cells reveals potential intervention targets for plasma cell neoplasia. *Blood* 2012; **119**: 1018–1028.
- 41 Cook RT, Schlueter AJ, Coleman RA, Tygrett L, Ballas ZK, Jerrells TR *et al*. Thymocytes, pre-B cells, and organ changes in a mouse model of chronic ethanol ingestion—absence of subset-specific glucocorticoid-induced immune cell loss. *Alcohol Clin Exp Res* 2007; **31**: 1746–1758.
- 42 Boyden AW, Legge KL, Waldschmidt TJ. Pulmonary infection with influenza A virus induces site-specific germinal center and T follicular helper cell responses. *PLoS One* 2012; **7**: e40733.
- 43 Suematsu S, Matsuda T, Aozasa K, Akira S, Nakano N, Ohno S *et al*. IgG1 plasmacytosis in interleukin 6 transgenic mice. *Proc Natl Acad Sci USA* 1989; **86**: 7547–7551.
- 44 Kupperman E, Lee EC, Cao Y, Bannerman B, Fitzgerald M, Berger A *et al*. Evaluation of the proteasome inhibitor MLN9708 in preclinical models of human cancer. *Cancer Res* 2010; **70**: 1970–1980.
- 45 Tian Z, Zhao JJ, Tai YT, Amin SB, Hu Y, Berger AJ *et al*. Investigational agent MLN9708/2238 targets tumor-suppressor miR33b in MM cells. *Blood* 2012; **120**: 3958–3967.
- 46 Fendrich V, Schneider R, Maitra A, Jacobsen ID, Opfermann T, Bartsch DK. Detection of precursor lesions of pancreatic adenocarcinoma in PET-CT in a genetically engineered mouse model of pancreatic cancer. *Neoplasia* 2011; **13**: 180–186.
- 47 Heijink DM, Kleibeuker JH, Nagengast WB, Oosterhuis D, Brouwers AH, Koomstra JJ *et al*. Total abdominal 18F-FDG uptake reflects intestinal adenoma burden in Apc mutant mice. *J Nucl Med* 2011; **52**: 431–436.
- 48 Walter MA, Hildebrandt IJ, Hacke K, Kesner AL, Kelly O, Lawson GW *et al*. Small-animal PET/CT for monitoring the development and response to chemotherapy of thymic lymphoma in Trp53 –/– mice. *J Nucl Med* 2010; **51**: 1285–1292.
- 49 Shortt CP, Gleeson TG, Breen KA, McHugh J, O'Connell MJ, O'Gorman PJ *et al*. Whole-body MRI versus PET in assessment of multiple myeloma disease activity. *AJR Am J Roentgenol* 2009; **192**: 980–986.
- 50 Zechmann CM, Trainee L, Meissner T, Wagner-Gund B, Giesel FL, Goldschmidt H *et al*. Parametric histogram analysis of dynamic contrast-enhanced MRI in multiple myeloma: a technique to evaluate angiogenic response to therapy? *Acad Radiol* 2012; **19**: 100–108.
- 51 Nakamoto Y, Kurihara K, Nishizawa M, Yamashita K, Nakatani K, Kondo T *et al*. Clinical value of (11)C-methionine PET/CT in patients with plasma cell malignancy: comparison with (18)F-FDG PET/CT. *Eur J Nucl Med Mol Imaging* 2013; **40**: 708–715.
- 52 Brepoels L, Stroobants S, Verhoef G, De Groot T, Mortelmans L, De Wolf-Peeters C. (18)F-FDG and (18)F-FLT uptake early after cyclophosphamide and mTOR inhibition in an experimental lymphoma model. *J Nucl Med* 2009; **50**: 1102–1109.



This work is licensed under a Creative Commons Attribution-NonCommercial-ShareAlike 3.0 Unported License. To view a copy of this license, visit <http://creativecommons.org/licenses/by-nc-sa/3.0/>

Supplementary Information accompanies this paper on Blood Cancer Journal website (<http://www.nature.com/bcj>)